Piezooptics in Non-Uniform Mechanical Fields

Piezooptics in Non-Uniform Mechanical Fields

By

Rostyslav Vlokh, Igor Skab,
Oleh Krupych and Dmitro Adamenko

Cambridge
Scholars
Publishing

Piezooptics in Non-Uniform Mechanical Fields

By Rostyslav Vlokh, Igor Skab, Oleh Krupych and Dmitro Adamenko

This book first published 2022

Cambridge Scholars Publishing

Lady Stephenson Library, Newcastle upon Tyne, NE6 2PA, UK

British Library Cataloguing in Publication Data
A catalogue record for this book is available from the British Library

ISBN (10): 1-5275-7689-2
ISBN (13): 978-1-5275-7689-6

TABLE OF CONTENTS

INTRODUCTION

The discovery of the effects of parametric optics, in particular, the piezooptic effect by D. Brewster in 1818 [1, 2], the magnetooptic effect by M. Faraday in 1845 [3], quadratic and linear electrooptic effects by Kerr and Pockels in 1875 and 1893, respectively [4, 5, 6] and the electrogyration effect by O.G. Vlokh in the second half of the XX century [7], took place over almost two centuries, which were associated primarily with significant experimental difficulties of studying these subtle phenomena. In addition, the absence of a symmetry-tensor apparatus of crystal physics had a significant effect on the long duration of this process. So, the equations for optical indicatrix deformation under the electrooptic effect for all point symmetry groups were obtained only in the 60s of the XX century [8, 9].

Despite the classical nature of the phenomena of parametric optics, they still remain the fundamental basis for the development of various optical devices. In particular, the photoelastic effect has long been used for non-destructive control of mechanical stresses of transparent optical elements, parts, and structures (including in tensor tomography), measurement of mechanical stress or pressure by a non-contact method, modulation of the state of polarization of optical radiation, and the like. In turn, in recent years, it has turned out that acoustooptic control of light radiation can be used in the capture of microparticles with an optical beam and manipulating them, for addressing optical beams that have various quantum states, in the framework of quantum cryptography and optical computer information processing, as well as in formation of a Bose-Einstein condensate [10].

The above circumstances make the further development of piezooptic materials science important and relevant. However, the existing experimental methods for studying the piezooptic properties of crystals are quite imperfect and lead to significant errors, which, in turn, does not allow to derive the most effective geometries in certain anisotropic crystalline materials.

This monograph is intended to familiarize the reader with the 2D-polarimetric and interferometric methods developed by the authors of the study of the piezooptic effect under the action of inhomogeneous mechanical stresses which have in advance known distribution across the

sample (namely, diametrical compression, mechanical torsion, and four-point bending). In addition, the monograph presents the results of experimental studies of the photoelastic properties of crystals, which provide for the determination of complete matrices of piezooptic and elastooptic coefficients.

SECTION 1

FUNDAMENTALS OF PHOTOELASTICITY. ANALYSIS OF STRESS HOMOGENEITY IN SAMPLES IN CLASSICAL PIEZOOPTIC EXPERIMENTS

1.1. Photoelasticity as a phenomenon of parametric optics

In the most general case, photoelasticity is an effect of changes in the refractive indices of optical medium under the influence of mechanical strains. Today, the phenomenon of photoelasticity is widely used in many fields of science and technology, in particular when checking mechanical stresses in transparent bodies [11–13], in remote optical sensors of stresses [14] and accelerometers [15–17], tensor-field stress tomography [18–22], and polarizing optical modulators [23, 24]. Moreover, of great importance is utilization of the photoelastic effect in various acoustooptic devices (deflectors, modulators, spectral filters, etc.), which are widely used in many modern techniques [25–28]. In addition, the photoelastic properties of materials should be taken into account when developing electrooptic devices. Practical applications of the photoelasticity effect mentioned above require complete and thorough information on so-called piezooptic and elastooptic coefficients.

The photoelasticity can be termed as "ancient" among various phenomena of parametric optics (i.e., the optics of media in external or internal fields). The first description of the photoelastic effect in optically isotropic media, amorphous solids and cubic crystals has been made by David Brewster at the beginning of the 19^{th} century [1, 2]. Within the framework of this theory, an optical birefringence Δn induced by a mechanical stress σ is expressed as follows:

$$\Delta n = K\sigma. \tag{1.1}$$

Different terms are used to denote the K coefficient. In particular, it is called a Brewster constant, a relative piezooptic coefficient, a relative photoelastic coefficient, or a stress-optical coefficient. The latter term is chiefly used by manufacturers of optical glass as a standard characteristic of any optical material [29, 30].

Since the scalar equation (1.1) is valid only for optically isotropic materials, one has to pass to a tensor relation in a more general case of anisotropic material. This relation has been suggested by Pockels [6]:

$$\delta B_{ij} = \sum_{k=1}^{3}\sum_{l=1}^{3} \pi_{ijkl}\sigma_{kl} \quad (i, j, k, l = 1\ldots3), \tag{1.2}$$

where δB_{ij} is the increment of dielectric impermeability tensor component (a so-called tensor of optical polarization constant) B_{ij} and σ_{kl} denote the component of mechanical stress tensor, and π_{ijkl} the tensor component of piezooptic coefficients, which is measured in the units of $m^2/N = Pa^{-1} = 10^{12}$ B (B = Brewster).

Neglecting the phenomena associated with antisymmetricity of the dielectric impermeability and the mechanical stress tensors (i.e., in the approximation $B_{ij} = B_{ji}$ and $\sigma_{kl} = \sigma_{lk}$), one can rewrite equation (1.2) in a matrix form (or a Voigt notation):

$$\delta B_{\lambda} = \pi_{\lambda\mu}\sigma_{\mu} \quad (\lambda, \mu = 1\ldots6), \tag{1.3}$$

where $\sigma_1 = \sigma_{11}$, $\sigma_2 = \sigma_{22}$, $\sigma_3 = \sigma_{33}$, $\sigma_4 = \sigma_{23}$, $\sigma_5 = \sigma_{13}$ and $\sigma_6 = \sigma_{12}$, $\delta B_1 = \delta B_{11}$, $\delta B_2 = \delta B_{22}$, $\delta B_3 = \delta B_{33}$, $\delta B_4 = \delta B_{23}$, $\delta B_5 = \delta B_{13}$ and $\delta B_6 = \delta B_{12}$, $\pi_{\lambda\mu} = \pi_{ijkl}$ if $\mu = 1\ldots3$ and $\pi_{\lambda\mu} = 2\pi_{ijkl}$ if $\mu = 4\ldots6$. Here and below, the Einstein rule is used for summation over repeating indices.

Equations (1.2) and (1.3) are mathematical formulations of the piezooptic effect. If the values δB_{λ} are expressed through mechanical strains, the term "elastooptic effect" is mainly used. In the matrix form, it can be written as

$$\delta B_{\lambda} = p_{\lambda\mu}\varepsilon_{\mu} \quad (\lambda, \mu = 1\ldots6), \tag{1.4}$$

where $p_{\lambda\mu}$ and ε_{μ} are the components of elastooptic coefficients and mechanical strain tensors, respectively.

It is known that the mechanical strain tensor and the mechanical stress tensor are coupled via the Hooke's law:

$$\varepsilon_\mu = S_{\mu\theta}\sigma_\theta, \tag{1.5}$$

$$\sigma_\mu = C_{\mu\theta}\varepsilon_\theta, \tag{1.6}$$

where $S_{\mu\theta}$ and $C_{\mu\theta}$ are the components of elastic compliance and elastic stiffness tensors, respectively.

Thus, the piezooptic and elastooptic coefficients are coupled through the $S_{\mu\theta}$ and $C_{\mu\theta}$ tensors:

$$\begin{aligned} \pi_{\lambda\mu} &= p_{\lambda\theta}S_{\theta\mu}, \\ p_{\lambda\mu} &= \pi_{\lambda\theta}C_{\theta\mu}. \end{aligned} \tag{1.7}$$

Therefore, by determining experimentally the complete matrices of two of the four tensors involved in the relations (1.7), one can calculate the two other tensors.

The values δB_λ can be expressed through a change in the refractive indices, using the relation $B_q = (n_q)^{-2}$ and differentiating it:

$$\delta B_q = -\frac{2}{n_q^3}\delta n_q. \tag{1.8}$$

Here n_q implies the initial refractive index and δn_q the change in the refractive index occurring due to mechanical stresses (or strains).

Substituting formula (1.8) into (1.3) and (1.4), one obtains the relation that links the δn_q values with the mechanical stresses or strains:

$$\begin{aligned} \delta n_q &= -\frac{1}{2}n_q^3\pi_{qm}\sigma_m = K_{qm}\sigma_m, \\ \delta n_q &= -\frac{1}{2}n_q^3 p_{qm}\varepsilon_m, \end{aligned} \tag{1.9}$$

where K_{qm} denotes the photoelastic coefficient.

It follows from the relation (1.3) that, in general, the piezooptic tensor (as well as the elastooptic one) can be represented by a 6×6 matrix, which contains 36 independent coefficients. For a convenience, this matrix is usually divided into four sub-matrices **A**, **B**, **C** and **D**:

$$\pi_{qm} = \left[\begin{array}{ccc:ccc} \pi_{11} & \pi_{12} & \pi_{13} & \pi_{14} & \pi_{15} & \pi_{16} \\ \pi_{21} & \pi_{22} & \pi_{23} & \pi_{24} & \pi_{25} & \pi_{26} \\ \pi_{31} & \pi_{32} & \pi_{33} & \pi_{34} & \pi_{35} & \pi_{36} \\ \hdashline \pi_{41} & \pi_{42} & \pi_{43} & \pi_{44} & \pi_{45} & \pi_{46} \\ \pi_{51} & \pi_{52} & \pi_{53} & \pi_{54} & \pi_{55} & \pi_{56} \\ \pi_{61} & \pi_{62} & \pi_{63} & \pi_{64} & \pi_{65} & \pi_{66} \end{array}\right] = \begin{bmatrix} \mathbf{A} & \mathbf{B} \\ \mathbf{C} & \mathbf{D} \end{bmatrix}, \tag{1.10}$$

$$\mathbf{A} = \begin{bmatrix} \pi_{11} & \pi_{12} & \pi_{13} \\ \pi_{21} & \pi_{22} & \pi_{23} \\ \pi_{31} & \pi_{32} & \pi_{33} \end{bmatrix}, \mathbf{B} = \begin{bmatrix} \pi_{14} & \pi_{15} & \pi_{16} \\ \pi_{24} & \pi_{25} & \pi_{26} \\ \pi_{34} & \pi_{35} & \pi_{36} \end{bmatrix},$$
$$\mathbf{C} = \begin{bmatrix} \pi_{41} & \pi_{42} & \pi_{43} \\ \pi_{51} & \pi_{52} & \pi_{53} \\ \pi_{61} & \pi_{62} & \pi_{63} \end{bmatrix}, \mathbf{D} = \begin{bmatrix} \pi_{44} & \pi_{45} & \pi_{46} \\ \pi_{54} & \pi_{55} & \pi_{56} \\ \pi_{64} & \pi_{65} & \pi_{66} \end{bmatrix}. \tag{1.11}$$

The sub-matrix **A** includes the "principal" piezooptic coefficients that describe the changes in the principal components of the dielectric impermeability tensor (δB_1, δB_2 and δB_3). This corresponds to the change in the ellipsoid of refractive indices (or the so-called optical indicatrix) that occurs along the principal coordinate axes under the action of stretching or compressing stresses (i.e., under the action of normal components σ_1, σ_2 and σ_3 of the mechanical stress tensor). The sub-matrix **B** contains the "shift" (or "shifting") piezooptic coefficients that describe the changes in the optical indicatrix under the action of shear (shift) stresses (i.e., the shear components σ_4, σ_5 and σ_6 of the mechanical stress tensor). Finally, the "rotating" (see the sub-matrix **C**) and the "rotating-shifting" (the sub-matrix **D**) piezooptic coefficients describe the changes in the "rotating" components δB_4, δB_5 and δB_6 of the dielectric impermeability tensor (i.e., those that cause rotation of the optical indicatrix) under the action of normal (σ_1, σ_2 and σ_3) and shear (σ_4, σ_5 and σ_6) components of the mechanical stress tensor, respectively.

Symmetry of a material medium allows for reducing the number of independent components of the piezooptic and elastooptic tensors. In particular, the matrix (1.10) contains only twelve nonzero coefficients in case of an amorphous (glassy) material, of which only two coefficients are independent:

$$\pi_{qm} = \left[\begin{array}{ccc:ccc} \pi_{11} & \pi_{12} & \pi_{12} & 0 & 0 & 0 \\ \pi_{12} & \pi_{11} & \pi_{12} & 0 & 0 & 0 \\ \pi_{12} & \pi_{12} & \pi_{11} & 0 & 0 & 0 \\ \hdashline 0 & 0 & 0 & (\pi_{11}-\pi_{12}) & 0 & 0 \\ 0 & 0 & 0 & 0 & (\pi_{11}-\pi_{12}) & 0 \\ 0 & 0 & 0 & 0 & 0 & (\pi_{11}-\pi_{12}) \end{array}\right]. \qquad (1.12)$$

For the crystals that belong to the cubic system, the number of independent components of the piezooptic and elastooptic tensors increases to three or four, while for the hexagonal system we have from six to eight components. In the same way, one can obtain seven to ten independent components for the tetragonal system, eight to twelve for the trigonal system, twelve for the orthorhombic system, twenty for the monoclinic system, and thirty six for the triclinic one.

1.2. Polarimetric method for measuring photoelastic constants

In experimental mechanics and glass production, various polarimetric methods [31–36] are commonly used to investigate photoelasticity properties. Historically, most of these methods have used visual or photographic recording of image of a sample, which is obtained in polarized light. At the end of the twentieth century, solid-state digital video cameras and computer technologies has been developed and widely spread. This has started production of the polarimeters for determining stress-induced optical birefringence, which are based upon digital image processing [37–43].

Over the past two decades, a number of 2D polarimeters (or imaging polarimeters) have been built at the O. G. Vlokh Institute of Physical Optics (Lviv, Ukraine) for the visible and infrared spectral ranges. All of them represent modifications of a basic 2D polarimeter configuration (Fig. 1-1) [44, 45]. This scheme includes a radiation source, a polarization generator, a sample under analysis, an analyzer, and an electronic section.

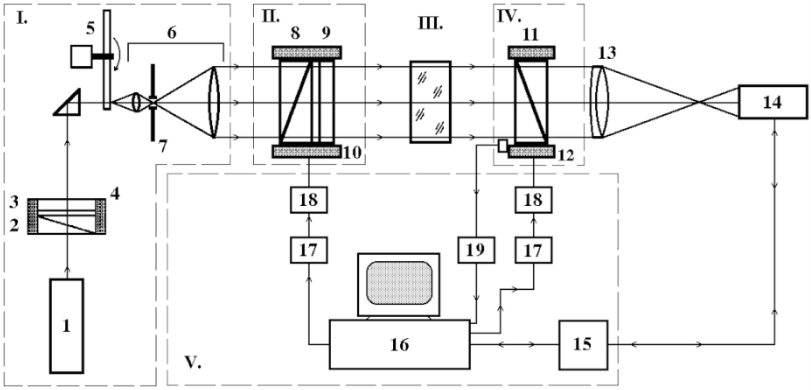

Fig. 1-1. Basic configuration of 2D polarimeter:
(I) radiation source: (1) gas laser, (2) linear polarizer, (3) quarter-wave plate, (4) rotation device, (5) coherence scrambler, (6) beam expander, (7) spatial filter;
(II) polarization generator: (8) linear polarizer, (9) quarter-wave plate, (10) rotation device,
(III) sample under analysis;
(IV) analyzer: (11) linear polarizer, (12) rotation device;
(V) electronic section: (15) video camera interface, (16) computer, (17) stepper motor controller, (18) stepper motor, (19) zero-position sensor controller of analyzer.
Adapted with permission from Vasylkiv, Y., Kvasnyuk, O., Krupych, O., Mys, O., Maksymuk, O., & Vlokh, R. (2009). Reconstruction of 3D stress fields basing on piezooptic experiment. Ukr. J. Phys. Opt., 10(1), 22–37. © O. G. Vlokh Institute of Physical Optics.

Now let us describe in brief the main sections of this configuration.

Radiation source. The objective of this section is to create an almost plane monochromatic light wave with circular polarization and controlled intensity. It includes a gas laser (1), a radiation-intensity controller (2)–(4), a coherence scrambler (5) and a beam expander (6) with a pinhole spatial filter (7). In our scheme, a helium-neon laser emits a monochromatic linearly polarized light with the wavelength 632.8 nm and the power 3 mW.

A radiation-intensity controller consists of a linear polarizer, i.e. a Glan prism (2) and a quarter-wave plate (3). Note that the fast axis of the quarter-wave plate makes the angle 45 deg with the transmission axis of polarizer. Taken together, these components form a circular polarizer, which is placed on a rotation device (4), which makes it possible to adjust the intensity of the incident light by rotating the circular polarizer around the axis of light beam. This rotation is controlled by a stepper motor.

After the radiation-intensity controller, the light beam passes through a coherence scrambler (5). The aim of this device is eliminating undesirable speckle patterns in the image, which arise from the interference of coherent laser light diffracted at the components of optical scheme. The coherence scrambler represents a grounded glass disk that scatters light with a speckle structure. This speckle structure is changing continuously, since this disk is being rotated using an electric motor. As a result of averaging that occurs during exposure of sample, the effect of "spotting" disappears and an improved image arises, which is like the image obtained with incoherent light.

After that, the light beam enters a beam expander (6), which is built according to a reciprocal Keppler telescopic system. To "clean" the beam from scattered and diffracted light, a spatial filter (7) (i.e., a pinhole diaphragm) is installed behind the first short-focus lens at the waist place. At the output of the beam expander, a collimated light beam with the diameter ~ 20 mm is obtained.

Hence, utilization of laser radiation source in the 2D polarimeter provides a high degree of monochromaticity and, at the same time, the coherence scrambler eliminates the speckle structure of images, which would have been otherwise inherent for the polarimetric systems based on monochromatic sources.

Finally, a high-quality collimated beam of circularly polarized light is obtained at the output of this section. This decreases any noises and increases the measurement accuracy.

Polarization generator. The objective of this section is to create a predetermined polarization state of the light wave, which is given by the azimuth and the ellipticity, at the entrance of sample. It includes a first linear polarizer (a Glan prism (8)) and a compensator (a quarter-wave plate (9)).

The ellipticity K of the light wave at the output of the polarization generator is determined by the angle φ between the fast axis of the compensator and the transmission axis of the linear polarizer. The actual value of the optical phase difference of the compensator Γ_c is slightly different from its ideal value of 90 deg. Then the actual value of the ellipticity K reads as

$$K = \tan(\varepsilon),\ \varepsilon = \frac{1}{2}\operatorname{asin}[\sin(\Gamma_c)\sin(2\varphi)], \tag{1.13}$$

where ε is the ellipticity angle. The azimuth θ of the polarization ellipse is determined by the angular position of the fast axis c and the Γ_c value:

$$\theta = c + \delta c,\ \tan(2\delta c) = \cos(\Gamma_c)\ \tan(2\varphi). \tag{1.14}$$

Here δc implies the azimuth correction associated with imperfections of the compensator.

Since the azimuth p of the linear polarizer and the angle φ between the transmission axis of the linear polarizer and the fast axis of the compensator are directly set during experiment, the parameter c becomes

$$c = p + \varphi. \tag{1.15}$$

Hence, by rotating the composite elliptical polarizer consisting of the linear polarizer and the compensator, any prescribed azimuth θ of the major axis of the polarization ellipse and any ellipticity K of the polarization can be set at the output.

A rotary device (10) enables rotation of the compensator (9) with respect to the linear polarizer (8), as well as joint rotation of the two latter components around the optical axis of the 2D polarimeter. Note that the composite elliptical polarizer is rotated by a stepper motor. As a consequence, the section of polarization generator provides a range of all possible azimuths from 0 to 180 deg and the range of ellipticities from –1 to +1.

Sample under test. Besides of a sample itself, this section also contains some additional devices. In particular, this can be a cuvette with immersion liquid, a device for rotating the sample or a loading device. The dimensions of the analyzed area of sample are determined by the diameter of collimated light beam at the output of the composite elliptical polarizer. In its turn, this diameter is given by the linear dimensions of the Glan polarization prism (8) and equals to ~ 20 mm.

Analyzer. The objective of this section is to analyze the polarization state of the light beam at the output of the sample. It comprises a second linear polarizer (a Glan prism (11)) arranged at a rotation device (12), which is controlled by a stepper motor. The rotation device is equipped with a zero-position sensor connected to a computer. This is due to a need in setting precisely a laboratory coordinate system when determining the azimuth angles.

After the light has passed through the analyzer, the image of spatial intensity distribution over the light beam section is formed, by means of a lens (13), in the plane of photosensitive matrix of a detector, a video camera (14). For example, it can be a camera based on a charge-coupled device. Then the sensitive area of the photodetector contains 795 horizontal and 596 vertical elements. The choice of the lens mentioned above depends on the

size of the sample under test, the resolution of the photodetector and the overall dimensions of the 2D polarimeter.

Electronic section. This section includes a video-camera interface (15), a computer (16), stepper-motor controllers (17), stepper motors (18) and a zero-position sensor controller of an analyzer (19). The interface of the video camera (15) provides reading the image of the intensity distribution line by line, digitizing it and transferring the corresponding data to the computer memory. According to control signals, the stepper-motor controllers (17) generate sequences of pulses, that are fed to windings of the stepper motors (18). They determine the directions of rotation of motors and the rotation angles

In the 2D polarimeter presented above, the rotary stages have the minimum rotation step of 0.012 deg and the accuracy 0.001 deg of angular positioning. Finally, the computer (16) carries out the operation control of all the elements of the polarimeter according to a preset measurement algorithm, accumulates and processes the data, and presents and saves the experimental results.

Original software of the 2D polarimeter forms a shell for controlling its work. In particular, it controls the stepper motors, reads the image from the video camera, presents it on the computer display, processes the overall image and the data for a certain image pixel, fits the data for angular dependences with the sine function, initialize the analyzer; "binds" the polarizer to the analyzer, calibrates the image shift arising from the analyzer rotations, implements the algorithm of polarization-optical measurements, and calculates the resultant Jones matrix of the optical system. Moreover, it enables one to control the 2D polarimeter in manual and automatic measurement mode.

The basic configuration of the 2D polarimeter considered above is universal in the sense that it provides implementing different methods for measuring the parameters of optical anisotropy, depending on the complexity of task designated by experimenter.

1.3. Non-uniformity of mechanical stresses in a sample under axial compression

A significant negative aspect of photoelasticity studies is that the piezooptic coefficients $\pi_{\lambda\mu}$ of crystals are usually measured with large errors. Quite often, the latter exceed tens of percents and, in some cases, become as large as the value of the coefficient itself (see, e.g., Refs. [46–48]).

To understand the reasons for this disappointing situation, one has to analyze a typical scheme of traditional photoelastic measurements

performed in crystal optics. For instance, the sample to which axial compression is applied has usually a shape of a parallelepiped close to a cube [49]. Usually, a strained sample is placed into a single-beam polarimeter or a double-arm interferometer (e.g., Michelson or Mach–Zender interferometers). Then the sample is irradiated by a laser beam with the diameter ~ 1 mm. As a rule, the mechanical strain is changed during the experiment in order to measure a so-called "half-wave mechanical strain". It is obvious that these experimental procedures contain a number of possible sources of measurement errors.

1.3.1. Experimental procedures and results

In order to visualize better the sources of measurement errors of the piezooptic coefficients, we use the same basic configuration of the 2D polarimeter [45] (see Fig. 1-1) and the measurement technique presented in the work [50]. To perform the measurements, the quarter-wave plate (9) is oriented so that its fast axis forms the angle 45 deg with the transmission axis of the polarizer (8). Then the circularly polarized light is formed at the output of the polarization generator. This light is incident on the sample which is prepared in the shape of a plane-parallel plate.

The propagation of light through the sample changes the state of light polarization. To determine the polarization state of the light emerged from the sample, the analyzer is rotated in the angular range from 0 to 180 deg with the step of 4.5 deg. Note that the sample image is recorded for every azimuthal position of the analyzer. Once the analyzer has reached the angle 90 deg, the light beam is shut out and the background image is recorded. The overall time of the measuring procedure is less than 30 seconds.

In case when the circularly polarized light enters the sample as described by the model of linear optical retarder, the light intensity I at the analyzer output is determined by the formula

$$I = \frac{I_0}{2}\left\{1+\sin\Gamma\sin\left[2\left(a-\zeta\right)\right]\right\}, \tag{1.16}$$

with I_0 being the intensity of light incident on the sample, a the azimuth of the transmission axis of polarizer, ζ the orientation angle of the principal axes of cross-section of the optical indicatrix with the plane perpendicular to the light beam, $\Gamma = 2\pi\Delta/\lambda = 2\pi d(\Delta n)/\lambda$ the optical phase difference, Δ the optical retardation, λ the light wavelength, d the sample thickness, and Δn the optical birefringence.

After recording and filtering of the images, the azimuthal dependences of the intensity I are fitted by the sine function for each pixel:

$$I = C_1 + C_2 \sin\left[2\left(a - C_3\right)\right], \tag{1.17}$$

where C_1, C_2 and C_3 are fitting coefficients.

By comparing formulae (1.16) and (1.17), one can write out the fitting coefficients as follows:

$$C_1 = \frac{I_0}{2},\ C_2 = \frac{I_0}{2}\sin\left(\Gamma\right),\ C_3 = \zeta. \tag{1.18}$$

The Γ value is determined only by the fitting coefficients C_1 and C_2:

$$\sin\Gamma = \frac{C_2}{C_1}. \tag{1.19}$$

In its turn, the angular orientation of the intensity minimum is given by the orientation ζ of the principal axis of the optical indicatrix, which is equal to the coefficient C_3.

After fitting the light intensity for each pixel of the sample image behind the analyzer as a function of polarization azimuth, one can construct 2D maps of the optical anisotropy parameters for the sample. These parameters comprise the optical retardation Δ and the orientation angle ζ of the principal axis of the optical indicatrix.

As a demonstration of accuracy of our experiments, we present in Fig. 1-2 the spatial distributions of optical retardation and the orientation of the principal axis of the optical indicatrix for “empty” polarimeter with no sample inserted.

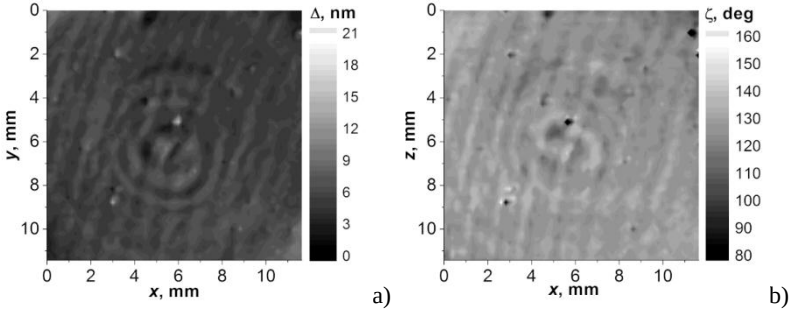

Fig. 1-2. Images of distributions of optical retardation (a) and orientation of major principal axis of the optical indicatrix (b), as measured for the polarimeter with no sample inserted into optical scheme.

Adapted with permission from Vasylkiv, Y., Kvasnyuk, O., Krupych, O., Mys, O., Maksymuk, O., & Vlokh, R. (2009). Reconstruction of 3D stress fields basing on piezooptic experiment. Ukr. J. Phys. Opt., 10(1), 22–37. © O. G. Vlokh Institute of Physical Optics.

Of course, the optical retardation for the air and isotropic optical elements such as lenses and polarizers should be equal to zero. However, some false "background" retardation still exists. It is due to experimental errors caused mainly by multiple light reflections in the optical elements and small misalignments of the optical axes of those elements, which are being rotated during the experiment. Following from the results presented in Fig. 1-2, one can determine the apparatus-driven errors in evaluating the optical retardation and the orientation of optical indicatrix. These are equal to ±3.5 nm and ±5 deg, respectively.

A loading device used in this experiment (see Fig. 1-3 and Ref. [50]) has been selected basing on the analysis [14, 15], which provides the most uniform distribution of stresses within the sample.

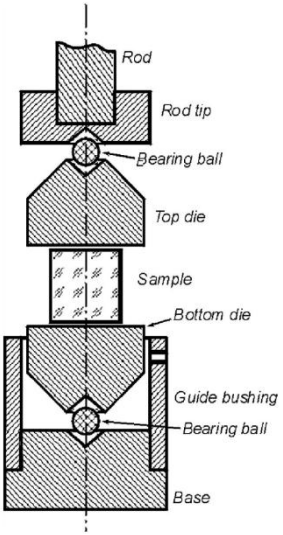

Fig. 1-3. Scheme of the loading device.
Note: We use a cardboard between the sample and the top (bottom) die as and intermediate layer, in order to eliminate inhomogeneity of the corresponding surfaces and decrease the friction force between these surfaces.
Adapted with permission from Vasylkiv, Y., Kvasnyuk, O., Krupych, O., Mys, O., Maksymuk, O., & Vlokh, R. (2009). Reconstruction of 3D stress fields basing on piezooptic experiment. Ukr. J. Phys. Opt., 10(1), 22–37. © O. G. Vlokh Institute of Physical Optics.

The sample in the shape of cube with the dimensions $11.45(x)\times11.3(y)\times11.45(z)$ mm^3 has been prepared from a BK7 glass (according to Schott classification). Its refractive index at the light wavelength $\lambda = 632.8$ nm is equal to $n = 1.51466$, while the photoelastic coefficient $K = (n_0)^3(\pi_{11} - \pi_{12})/2$ at the wavelength $\lambda = 550$ nm is equal to $K = 2.76$ m^2/N [51]. The dispersion of the piezooptic coefficients in a narrow spectral region 550–632.8 nm has been neglected.

The distributions of the optical retardation and the orientation of principal axis of the optical indicatrix for the glass sample with no mechanical stress applied are presented in Fig. 1-4. It follows from these results that the residual optical birefringence Δn is smaller than 6×10^{-7}. Moreover, a comparison of the maps presented in Fig. 1-3 and Fig. 1-4 testifies that the major part of this birefringence is false, being caused by specific features of both the experimental setup and the method used. In other terms, we deal simply with an apparatus error. In fact, the

birefringence as small as $\Delta n \approx 6\times10^{-7}$ merely represents the accuracy for the birefringence achieved in the experiment.

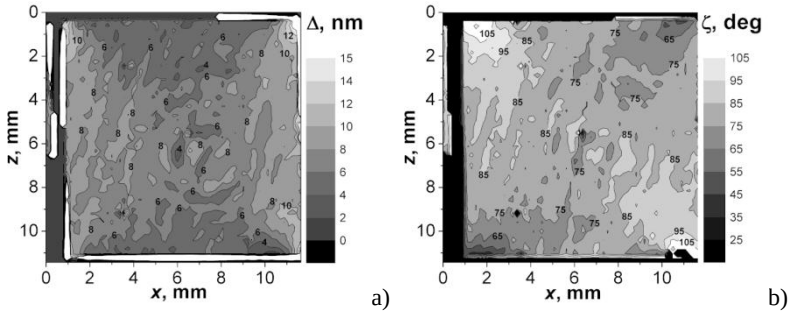

Fig. 1-4. Images of distributions of optical retardation (a) and orientation of principal axis of the optical indicatrix (b) for a glass sample with no mechanical stress applied.

Adapted with permission from Vasylkiv, Y., Kvasnyuk, O., Krupych, O., Mys, O., Maksymuk, O., & Vlokh, R. (2009). Reconstruction of 3D stress fields basing on piezooptic experiment. Ukr. J. Phys. Opt., 10(1), 22–37. © O. G. Vlokh Institute of Physical Optics.

Fig. 1-5 displays the distributions of the optical retardation and the orientation of principal axis of the optical indicatrix for the glass sample under conditions when the mechanical stress $\sigma_3 = -1.93\times10^6$ N/m^2 is applied. It is important that repeated experiments accompanied with realignments of sample have not led to notable difference in the distributions of optical parameters. However, the maximum of the optical retardation has become located at different points. Namely, it has been close to the lateral, upper or bottom edges of the sample in different experiments. These shifts are probably caused by some misalignments of stress-application scheme, which lead to appearance of additional components of the stress tensor.

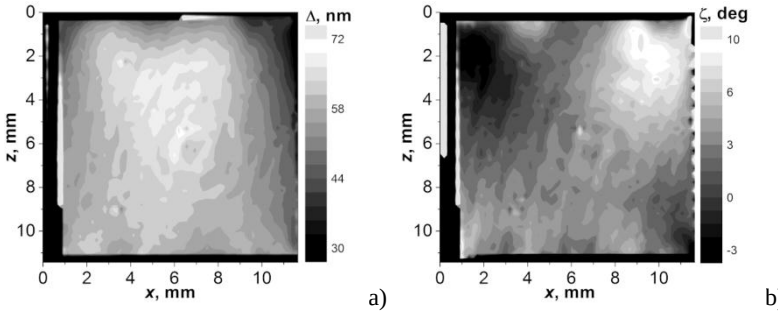

Fig. 1-5. Images of distributions of optical retardation (a) and orientation of principal axis of the optical indicatrix (b) for a glass sample under the mechanical stress $\sigma_3 = -1.93\times10^6$ N/m^2 applied.

Adapted with permission from Vasylkiv, Y., Kvasnyuk, O., Krupych, O., Mys, O., Maksymuk, O., & Vlokh, R. (2009). Reconstruction of 3D stress fields basing on piezooptic experiment. Ukr. J. Phys. Opt., 10(1), 22–37. © O. G. Vlokh Institute of Physical Optics.

The optical phase differences within the cross-section of the sample and the cross-section of laser beam (with the diameter 1.5 mm) propagating through the center of the cross-section are compared in Table 1-1. The relative error for the optical retardation inside the whole cross-section of the sample reaches the magnitude of 14%, while the relative error for the circular cross-section of laser beam is about 4%. In other words, the error for the experiments with non-expanded laser beam can be reduced at least by 3.5 times under condition that the mechanical stress in the spatial region where the laser beam propagates is known in advance.

Table 1-1. Optical retardation for the whole cross-section of sample and the cross-section of laser beam propagating through the sample center

Number of the experiment	Retardation for the whole cross-section of sample			Retardation for the cross-section of laser beam		
	Mean value, nm	Absolute error, nm	Relative error, %	Mean value, nm	Absolute error, nm	Relative error, %
1	58.11	8.53	14.66	66.06	1.71	2.59
2	58.50	9.12	15.58	67.99	3.18	4.67
3	55.72	7.73	13.87	63.09	2.85	4.50
4	55.74	9.51	17.07	61.33	2.53	4.13
5	55.72	5.73	10.30	60.33	2.23	3.71
6	56.58	6.84	12.09	62.44	2.78	4.46
Mean value	56.72	7.91	13.94	63.54	2.55	4.01

1.3.2. Reconstruction of mechanical stresses. Mechanical model and numerical simulations

Let us assume that the experimental conditions provide a possibility for uniform application of mechanical load along the z direction of sample and that the sample is initially optically homogeneous and isotropic. Let the optical radiation propagate along the y direction. Then the inhomogeneity of mechanical stresses inside the sample can appear only due to a friction force between upper and lower sample surfaces and the intermediate cardboard layers. The maximal friction forces $dF_{\max}$ are proportional to the loading stress σ_3,

$$dF_{\max} = k\sigma_3 dS, \tag{1.20}$$

where $k = 0.22$ is the friction coefficient for the case of friction between the glass and the paper (see Ref. [52]), and dS denotes a small element of square of the sample surface.

The friction forces mentioned are directed from the lateral faces of sample to the central z axis (see Fig. 1-6), thus leading to appearance of barrel-shaped distortion of the sample under the compressive stress σ_3.

In the first approximation, one can take into account the following boundary conditions for this type of inhomogeneously stressed sample:

(1) $\sigma_1 = \sigma_2 = 0$ on the four lateral faces of sample;

(2) $\sigma_1^{\max} = \sigma_2^{\max} = k\sigma_3$ on the upper and lower faces;

(3) $\sigma_3 = -1.93\times10^6$ N/m^2 on all the faces in our experiment and simulations.

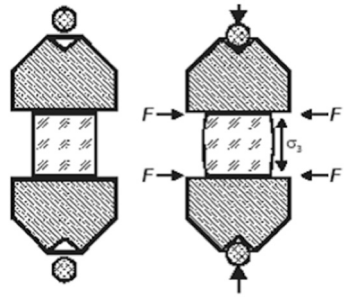

Fig. 1-6. Barrel-shaped distortion of sample under a compressive stress σ_3.
Adapted with permission from Vasylkiv, Y., Kvasnyuk, O., Krupych, O., Mys, O., Maksymuk, O., & Vlokh, R. (2009). Reconstruction of 3D stress fields basing on piezooptic experiment. Ukr. J. Phys. Opt., 10(1), 22–37. © O. G. Vlokh Institute of Physical Optics.

Let us use the approach presented in the work [53] for the superposition of three solutions, each of which being a solution of the problem for the elastic layer. The general solution of the Lame's equation in the absence of volume forces can be written as a sum of three solutions for the displacement vectors *u*, *v* and *w* along the *x*, *y* and *z* directions, respectively.

Simulations of the distribution of optical retardation have been performed on the basis of integral Jones matrix approach. The sample under analysis has been divided into 1000 (10×10×10) elementary (optically uniform) cells. The resulting Jones matrices $\mathbf{J}^{ij}$ for each of 100 elementary beams (i, j = 1...10) have been obtained by multiplying the Jones matrices of 10 elementary cells, through which each elementary beam has passed along the *y* direction:

$$\mathbf{J}^{ij} = \prod_{n=1}^{10} \mathbf{J}_n^{ij}. \tag{1.21}$$

Here $\mathbf{J}_n^{ij}$ is the Jones matrix of the elementary cell:

$$\mathbf{J}_n^{ij} = \begin{vmatrix} e^{i\Gamma_n^{ij}/2}\cos^2\zeta_n^{ij} + e^{-i\Gamma_n^{ij}/2}\sin^2\zeta_n^{ij} & i\sin(\Gamma_n^{ij}/2)\sin 2\zeta_n^{ij} \\ i\sin(\Gamma_n^{ij}/2)\sin 2\zeta_n^{ij} & e^{i\Gamma_n^{ij}/2}\sin^2\zeta_n^{ij} + e^{-i\Gamma_n^{ij}/2}\cos^2\zeta_n^{ij} \end{vmatrix}. \tag{1.22}$$

Γ_n^{ij} represents the optical phase difference of the elementary cell,

$$\Gamma_n^{ij} = \frac{\pi d_n^{ij}}{\lambda} n_0^3 (\pi_{11} - \pi_{12}) \sqrt{\left[(\sigma_1)_n^{ij} - (\sigma_3)_n^{ij}\right]^2 + \left[2(\sigma_5)_n^{ij}\right]^2}, \tag{1.23}$$

and ζ_n^{ij} denotes the angle of orientation of quasi-principal axes of the optical indicatrix,

$$\zeta_n^{ij} = \frac{1}{2}\operatorname{atan}\frac{2(\sigma_5)_n^{ij}}{(\sigma_1)_n^{ij} - (\sigma_3)_n^{ij}}. \tag{1.24}$$

Because the Jones vector of the elementary beam at the sample output reads as

$$\mathbf{E}_{out}^{ij} = \begin{pmatrix} E_1^{ij} \\ E_3^{ij} \end{pmatrix} = \mathbf{J}^{ij}\mathbf{E}_{circ},\ \mathbf{E}_{circ} = \frac{1}{\sqrt{2}}\begin{pmatrix} 1 \\ i \end{pmatrix}, \tag{1.25}$$

the resulting phase difference for each elementary beam is determined by the ratio

$$\Gamma^{ij} = \frac{\pi}{2} + \arg\left(\frac{E_1^{ij}}{E_3^{ij}}\right) = \frac{\pi}{2} - \arg\left(\frac{E_3^{ij}}{E_1^{ij}}\right). \tag{1.26}$$

Then the optical retardation $\Delta = \Gamma\lambda/2\pi$ can be calculated.

To match the calculated distribution of the optical retardation with the experimental one, it has been taken into account that the pressure on the upper face of sample has the form of half-period of the sinusoid shifted to the left, which corresponds to non-ideal setting of the sample:

$$\sigma_3\big|_{z=c} = -N_1\left[-0,05\sin\pi\frac{x}{a}\sin\pi\frac{y}{b} + 0,3\frac{\pi^2}{48}\left(1-\frac{x}{a}\right)\left(1-\frac{y}{b}\right)\right]. \tag{1.27}$$

In order to account for a barrel-shaped distortion, the stress on the side faces satisfies the boundary conditions

$$\begin{aligned} &\sigma_1\big|_{x=0,\,a} = 0, \quad \sigma_2\big|_{x=0,\,a} = -0.2\times\sigma_3\sin\pi\frac{z}{c}\sin\pi\frac{y}{b}, \\ &\sigma_2\big|_{y=0,\,b} = 0, \quad \sigma_1\big|_{y=0,\,b} = -0.2\times\sigma_3\sin\pi\frac{x}{a}\sin\pi\frac{z}{c}. \end{aligned} \tag{1.28}$$

Fig. 1-7 shows the simulation data for the piezo-induced optical retardation and orientation of optical indicatrix which takes into account a barrel-like deformation of the sample under pressure and inaccuracy of its setting with respect to the axis of pressure application.

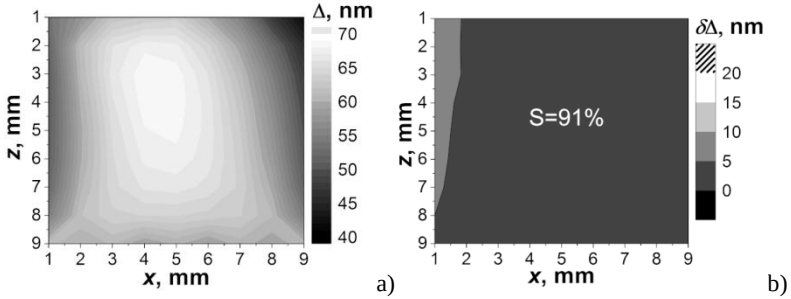

Fig. 1-7. Maps of simulated optical retardation (a) and difference of experimental (see Fig. 1-5a) and simulated optical retardations (b).
Adapted with permission from Vasylkiv, Y., Kvasnyuk, O., Krupych, O., Mys, O., Maksymuk, O., & Vlokh, R. (2009). Reconstruction of 3D stress fields basing on piezooptic experiment. Ukr. J. Phys. Opt., 10(1), 22–37. © O. G. Vlokh Institute of Physical Optics.

Fig. 1-7b indicates that the major part (91%) of the cross-section is correlated with the experimental results. Nonetheless, its small part (9%) still disagrees with the experimental data. It is probably caused by some warp of the top die in the upper left side of the sample, along with some sliding between the sample and the die. This can be accounted for while reducing the friction coefficient down to the value $k = 0.1$ (Fig. 1-8). In this case the experimental and simulation results have the similarity 98%.

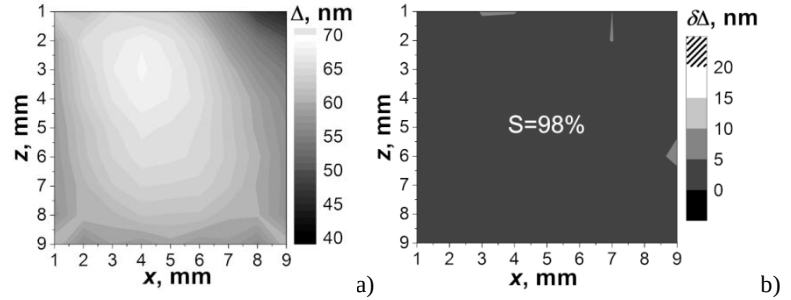

Fig. 1-8. Maps of simulated optical retardation (a) and difference of experimental (see Fig. 1-5a) and simulated optical retardations (b), as obtained after sliding between the sample and the die is taken into account.
Adapted with permission from Vasylkiv, Y., Kvasnyuk, O., Krupych, O., Mys, O., Maksymuk, O., & Vlokh, R. (2009). Reconstruction of 3D stress fields basing on piezooptic experiment. Ukr. J. Phys. Opt., 10(1), 22–37. © O. G. Vlokh Institute of Physical Optics.

By analyzing the simulated mechanical-stress distribution, the following conclusions can be made:

- loading of sample in a common manner gives rise not only to the component σ_3 of the mechanical stress tensor, but also to all the other components of this tensor;
- the distribution of mechanical stress tensor components inside the sample is inhomogeneous;
- the σ_3 component in the vicinity of geometrical center of the sample is one order of magnitude larger than the σ_1 component and two orders of magnitude larger than the other stress components;
- the σ_3 component in the center of the sample reaches a value 26% higher than the stress actually loaded, while the deviation of this component within the sample volume amounts to 32%;
- the deviations of the other stress components exceed hundred per cents and, moreover, the signs of the shift stress components are different in different parts of the sample.

Let us assume that a non-expanded laser beam with the cross-section area ~ 2 mm^2 propagates through the sample center parallel to the *y* axis. The optical phase difference for this light propagation direction is equal to 65.7 deg. On the other hand, the optical phase difference for the case of homogeneously distributed mechanical stress ($\sigma_3 = -1.93\times10^6$ N/m^2) can be calculated with the formula

$$\Gamma = 2\pi d n_0^3 \left(\pi_{11} - \pi_{12}\right)\sigma_3 / \lambda. \qquad (1.29)$$

It is equal to 60.1 deg. Hence, the actual value of the optical phase difference is smaller by 8.5% than the measured one. This means that in any practical piezooptic experiment, which does not take the distribution of mechanical stresses into account, the piezooptic coefficients determined experimentally differ from their actual values at least by 8.5%.

Of course, only complete reconstruction of the stress field inside a sample and a consistent consideration of the stress components at each sample point would allow one to obtain a correct value of the piezooptic coefficient. In our case the latter is equal to $(\pi_{11} - \pi_{12}) = 1.59\times10^{-12}$ m^2/N.

Summing up the results, we conclude that the greatest contribution into inhomogeneous distribution of mechanical stress originates from the imperfection of pressing surface of a poisson, the sample non-parallelism, and the friction between the poissons and the sample faces. At the same

time, the enormous errors appearing in typical piezooptic experiments are mainly caused by the friction forces that exist inside an intermediate contact layer between the upper and lower sample surfaces and the corresponding substrates, as well as by the misalignments of mechanical loading. The friction force leads to a barrel-shaped distortion of samples and the inevitable appearance of all components of the mechanical stress tensor, in spite of the fact that a uniaxial pressure has been initially applied.

Unlike the simplest experiment with an isotropic medium discussed above, the distribution of mechanical stresses in the case of anisotropic media will be even more complicated, and the requirements for the loading device and the sample more strict. A possible way out of this situation is to use the technique described above to investigate the piezooptic effect in crystals. It allows for determining the degree of inhomogeneity of the spatial field of mechanical stresses inside the sample and increasing the accuracy of the piezooptic coefficients.

It has been shown above that, instead of a uniform stress state which has traditionally been a priori supposed, uniaxial compressing of a parallelepiped-shaped sample results in a non-uniform distribution of mechanical stresses, with uncontrolled inhomogeneity. Therefore, it is almost impossible to obtain a uniform stress distribution when measuring piezooptic coefficients. Then it would be advisable to use such sample-loading methods which lead to a non-uniform, though known beforehand mechanical stress distribution.

1.4. Optimal geometric proportions of samples for piezooptic experiments

As shown above, the mechanical stress tensor components are non-uniformly distributed in any parallelepiped-shaped sample, even if a uniaxial compressing load is applied to this sample.

The reasons why a complicated spatial distribution of the stress components appears lie in misalignments of sample loading and a barrel-shaped distortion of rectangular samples. As a result, the error in determination of the mechanical stress tensor component σ_3 is about 30%. This error can be reduced down to ~ 14% by accurately aligning the sample in a pressure setup and carefully complying the condition of parallelism of the opposite sample surfaces. However, the barrel-shaped distortion, which appears due to the friction forces arising between the upper and lower sample surfaces and the appropriate substrates, cannot be eliminated completely.

To increase the accuracy of piezooptic experiments, we have suggested a number of methods for sample loading, which produce spatially inhomogeneous distributions of the stress components, of which coordinate dependences are known in advance. A diametrical compression of a disk, mechanical torsion of a rod and four-point bending of a bar are among these methods. They have turned out to be precise enough when determining the piezooptic coefficients. Moreover, some of them (e.g., the method of four-point bending) enables one to determine all of the piezooptic tensor components.

Nonetheless, these methods reveal a substantial practical disadvantage: they require a lot of samples with predetermined sizes and different crystallographic orientations. This necessitates growing of many (large enough) crystalline boules and utilizing complex procedures for manufacturing and precise processing the samples.

Returning to uniaxial compressing of a parallelepiped-shaped sample, one may ask the following questions:

- Could the loading-related errors of piezooptic experiments be minimized by optimizing a geometrical shape of a sample?
- Which are those optimal geometrical parameters of the sample and, first of all, the ratio of its width to its length, which make the errors caused by mechanical stress inhomogeneity inside the sample small or, at least, smaller than the errors typical for the polarimetric or interferometric experiments themselves?

One can try to solve this problem by means of simulations of the mechanical stress distributions in isotropic glass samples [54].

Let us consider a parallelepiped-shaped isotropic BK7-glass sample with a square cross-section ($a = b$) and different ratios of its width to height ($a : c$ = 1:1, 1:3 and 1:5). Let the compression load be applied along the z axis. Assume that the loading force is uniformly distributed over the upper and lower surfaces and the substrates are covered by a layer of paper. Then the coefficient of friction between the glass and the paper is equal to $k = 0.22$ [52]. Obviously, the friction forces appearing between the upper and lower sample faces and the substrates covered by the paper should lead to a barrel-shaped distortion of the sample.

The algorithm for solving the elastic equilibrium equation is similar to that used above. It has been described in detail in Refs. [50, 54]. Its application results in a spatial distribution of mechanical stress tensor components in the sample. Having obtained the distributions for all of the stress components, we have simulated the optical phase difference for the